Journal of Materials Chemistry C

ROYAL SOCIETY OF CHEMISTRY

PAPER

View Article Online
View Journal | View Issue

Cite this: J. Mater. Chem. C, 2022, 10, 2696

Doping of graphene *via* adlayer formation of electrochemically reduced dibenzyl viologen†

Thi Mien Trung Huynh,‡*[a] Thanh Hai Phan,‡[b] Roald Phillipson,[c] Alexander Volodine[d] and Steven De Feyter*[c]

Received 6th July 2021,
Accepted 19th September 2021

DOI: 10.1039/d1tc03142b

rsc.li/materials-c

In this contribution we demonstrate doping of graphene by uncharged dibenzyl viologen (DBV^0). Deposited electrochemically on chemical vapor deposited (CVD) graphene on SiO_2, DBV^0 forms a water-insoluble self-assembled molecular network, in contrast to water-soluble monocationic $DBV^{\bullet+}$. The phase formation at the molecular scale is revealed by scanning tunneling microscopy (STM) and atomic force microscopy (AFM). The doping efficiency is characterized by a combination of Raman spectroscopy and Kelvin probe force microscopy (KPFM). The Raman mapping of the G-band of the DBV^0 adlayer on top of CVD graphene on SiO_2 shows an apparent red shift compared to the unmodified analogue indicating an n-doping effect. This observation is in line with the KPFM results of which the measured contact potential difference (CPD) displays a positive shift compared to that of the pristine graphene.

Introduction

Graphene, a two-dimensional sp^2 hybridized carbon atom network, is of considerable interest as a new electronic material for both fundamental research and applications due to its unique electronic, optical, mechanical and thermal properties.[1,2] Despite these exceptional qualities one of the major drawbacks is its intrinsically low conductivity due to the negligible charge carrier density near the Dirac point. In addition, graphene is likely to show a p-type doping behavior at room temperature under ambient conditions.[3] Many studies aim at creating n-type doped graphene based on either atom substitution or adsorbate based protocols. A destructive approach by means of either replacing carbon atoms within the graphene lattice by nitrogen or boron[4–7] or creating covalent C–C bonds based on electrochemical grafting[8–16] causes a shift in the work function. However, this also disrupts the graphene lattice in an uncontrollable manner, thereby decreasing the charge carrier mobility.[17] Contrarily, functionalization by physisorption, a non-destructive protocol, provides an elegant method that preserves the carrier mobility as it does not affect the graphene lattice.[18–21] An attractive route towards controlled functionalization of graphene is *via* the formation of two-dimensional self-assembled molecular networks (2D-SAMNs).[22,23]

Among molecular building blocks, viologens (V) have attracted much attention in the field of surface electrochemistry since they can be applied as chromophores, electron-transfer mediators and gating molecules.[1,2,24–27] The reduced, uncharged species (V^0), has been recently recognized as an ideal n-dopant for various carbon nanostructures including nanotubes[28,29] and graphene[30] as well as for other 2D materials[31–36] as it has the lowest reduction potential among all electron-donor organic molecules. Accordingly, reduced viologen was chemically synthesized for doping purposes of graphene by reduction with $NaBH_4$ in toluene/water mix, followed by spin or dip coating on the substrate.[37] In contrast, *in situ* generation of the neutral viologen molecules *via* an electrochemical approach followed by adsorption on the substrate, as process that only takes few minutes has the additional advantage of control. In this mono-step synthesis, neutral viologen molecules are synthesized at the electrolyte/electrode interface, followed by their self-assembly onto the 2D material electrodes. Therefore, the target 2D materials are doped without any further treatments. However, as far as we are aware doping of 2D materials using this approach has not been reported yet.

In this study, we present a rapid and convenient approach for tuning the doping level of graphene by controlling the

[a] Quy Nhon University, Faculty of Natural Sciences, Department of Chemistry, 170 An Duong Vuong, Quy Nhon, Vietnam.
E-mail: huynhthimientrung@qnu.edu.vn
[b] Quy Nhon University, Faculty of Natural Sciences, Department of Physics, 170 An Duong Vuong, Quy Nhon, Vietnam
[c] KU Leuven, Department of Chemistry, Division of Molecular Imaging and Photonics, Celestijnenlaan 200F, Leuven B-3001, Belgium.
E-mail: steven.defeyter@kuleuven.be
[d] KU Leuven, Department of Physics, Division of Quantum Solid State Physics, Celestijnenlaan 200D, Leuven B-3001, Belgium

† Electronic supplementary information (ESI) available. See DOI: 10.1039/d1tc03142b

‡ These authors contributed equally to this work.

formation, *in situ*, of the neutral dibenzyl viologen species (DBV^0) on graphene. The method uses the electrochemical potential to govern the self-assembly of DBV^0 species on graphene as revealed by scanning tunneling microscopy (STM) and atomic force microscopy (AFM). The DBV^0 molecules strongly adsorb and form a striped pattern structure on graphene that causes a direct doping effect. The degree of doping is monitored *via* Kelvin probe force microscopy (KPFM) and Raman spectroscopy. The measured contact potential difference (CPD) revealed by KPFM displays a positive shift compared to that of pristine graphene suggesting n-doping of the DBV^0 films. This is further supported by the Raman mapping experiments that show an apparent red shift in the G-band of CVD graphene on SiO_2 upon being modified by the DBV^0 adlayer on top. The approach, based on the supramolecular self-assembly of electroactive molecules under electrochemical control, is an attractive alternative to dope graphene and other 2D materials.

Experimental

Materials and methods

Dibenzyl viologen (DBV) was purchased from Sigma-Aldrich and used without further purification. High purity water (Milli-Q, Millipore, TOC $<$ 3 ppb, resistivity $\geq$ 18.2 MΩ cm) was used for electrolyte preparation, including supporting electrolyte (50 mM HCl) and DBV^{2+}containing electrolyte (0.1 mM DBV^{2+} + 50 mM HCl). All electrolytes were deoxygenated with Ar gas (grade 5.0, Praxair) for several hours before use. Chemical vapor deposited (CVD) graphene on silicon dioxide (G-SiO_2) was purchased from Graphenea. Prior to each experiment, G-SiO_2 was cleaned by toluene. Highly oriented pyrolytic graphite (HOPG) substrates (ZYB grade, Momentive Performance Materials) were freshly cleaved using scotch tape. All cyclic voltammetry (CV) measurements and electrochemical deposition of DBV were carried out using an Autolab potentiostat (PGSTAT101, Metrohm–Autolab BV, the Netherlands) in combination with a lab-built single compartment three electrode cell with a useful volume of 38.5 mm^3. Pt wire placed in a glass compartment served as counter electrode. All potentials given in the text refer to a reversible hydrogen electrode (RHE). During the measurements, the electrolytes were kept under Ar.

Regarding the electrochemical deposition of DBV, graphitic surfaces exposed to the working electrolyte were polarized at the defined potentials for 180s. After deposition, the DBV modified graphitic samples were rinsed gently with Milli-Q (MQ) water to remove water-soluble species from the surface, and finally dried with an Ar stream.

Electrochemical (EC)-STM experiments were carried out with an apparatus designed at the University of Bonn as described elsewhere.[38] In order to eliminate the influence of oxygen as well as acoustic and electromagnetic interference, the entire EC-STM system is housed in a sealed aluminum chamber with electrical and liquid feedthroughs and filled with Ar. The EC-STM tips were electrochemically etched from 0.25 mm tungsten wire in 2 M KOH solution, rinsed with water, dried and subsequently coated by passing the tip through a lamella of hot-melt glue. The setpoint current (I_t) and bias voltage (U_b) are mentioned in the figure captions.

STM experiments were performed using a Molecular Imaging STM system, operating in constant-current mode. STM tips were prepared by mechanical cutting of Pt/Ir wire (80%/20%, diameter 0.25 mm). The bias voltage refers to the substrate. AFM measurements were carried out using a Multimode SPM (DI) with a Nanoscope IV controller. The AFM images were acquired in tapping mode under ambient air conditions with silicon cantilevers (spring constant of 21–60 N m^{-1}, resonance frequency of *ca.* 300 kHz, Olympus, Japan). STM and AFM data analysis was performed using WSxM 5.0.[39]

Raman measurements were performed with an OmegaScope 1000 (AIST-NT) with 632.8 nm He–Ne laser. The laser light was reflected by a long pass dichroic beam splitter (Chroma Technology Corporation, Z633RDC) and then focused onto the sample surface through an objective (MITUTOYO, BD Plan Apo 100X, N.A. 0.7) with 500 kW cm^{-2} optical density at the sample surface. Raman scattering was collected and directed to a Raman spectrograph (HoribaJY, iHR-320) equipped with a cooled-charge coupled device (CCD) camera operated at -100 °C (Andor Technology, DU920P) through the dichroic mirror, a pinhole and long pass filter (Chroma Technology Corporation, HQ645LP). For all samples, Raman maps were recorded before and after functionalization at 3 positions. Each map covers a 10 $\times$ 10 μm^2 area (10 $\times$ 10 pixels) and the accumulation time for each spectrum was 3 s. Outlying data points corresponding to bilayer graphene or defects are removed as described in ref. 40 All of the measurements were performed under ambient conditions.

KPFM measurements were performed in air using an Agilent 5500 scanning probe microscope using the amplitude modulation KPFM is a single-pass double frequency mode. For acquisition of the topographic images, the first resonance of the cantilever at 67 kHz was used. For KPFM, frequencies in the 10–30 kHz range were used for the ac voltage excitation of 1.5 V applied between the tip and sample. Commercial PPP-EFM probes from Nanosensors with tip radius $\sim$7 nm and a Pt/Ir conductive coating were used. The same tip was used to characterize the differently functionalized graphene samples.

Sample preparation for AFM, Raman and KPFM characterizations: G-SiO_2 and HOPG samples were exposed to the DBV^{2+} containing solution for 180s and polarized at the potentials facilitating the formation of desired redox states of DBV molecules. The samples were then dropwise rinsed with MQ water to remove water-soluble species, followed by conventional drying in an Ar flow and finally introduced to relevant systems for characterization.

Results and discussion

Dibenzyl viologens are well documented to form different self-assemblies on graphite and metallic surfaces depending on its redox states.[41–43] In our previous work, we demonstrated that

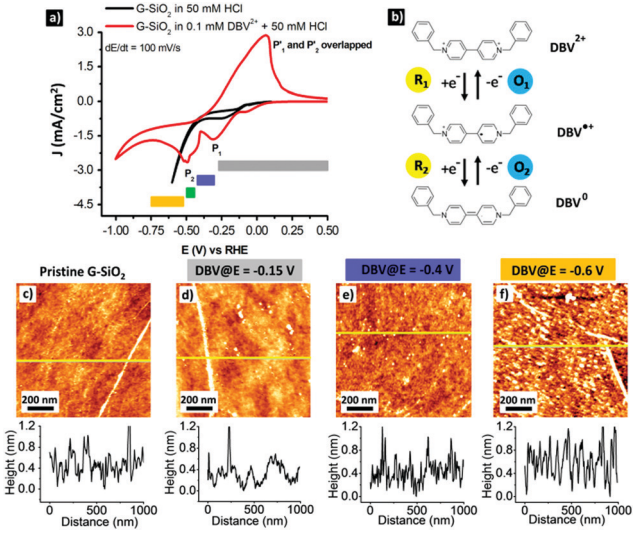

Fig. 1 (a) CVs of G-SiO_2 in 50 mM HCl (black trace) and in 0.1 mM DBV^{2+} + 50 mM HCl (red trace); (b) the redox states of DBV showing the transformation between dicationic, monocationic and uncharged species; AFM images and line profiles of (c) pristine G-SiO_2 and (d–f) DBV-functionalized G-SiO_2 prepared at different potentials. The root mean square (RMS) surface roughness of the corresponding surfaces is 0.27 nm, 0.26 nm, 0.29 nm and 0.47 nm, respectively. The RMS maximum at $E = -0.6$ V (f) is attributed to the deposition of the reduced DBV^0 species.

monocationic $DBV^{\bullet+}$ and uncharged DBV^0 molecules are capable of self-assembling on chemically modified graphite, forming the corresponding dimer and stacking structures under electrochemical control.[41] More importantly, unlike the $DBV^{\bullet+}$ based dimer pattern, the on-surface stacking structure formed by DBV^0 is water-insoluble.[44] This is attractive in view of air-stable doping of graphene. To realize this proof of concept, the electrochemical properties of a DBV containing electrolyte on G-SiO_2 were investigated.

Fig. 1a shows the cyclic voltammograms (CVs) of G-SiO_2 exposed to a supporting electrolyte (50 mM HCl) and DBV^{2+} containing solution (0.1 mM DBV^{2+} + 50 mM HCl). The CVs illustrate the respective potential windows limited by the hydrogen evolution reaction (HER) on the cathodic side. In the DBV containing solution, the on-set potential of the HER (red curve) is shifted negatively by $\Delta E = 0.4$ V in comparison with that in the supporting electrolyte (black curve). This observation indicates that the DBV adsorbed layer acts as a passive agent against the HER.[41,42,45] Importantly, the red CV is dominated by two main cathodic peaks, P_1 ($E_1 = -0.3$ V *vs.* RHE) and P_2 ($E_2 = -0.5$ V *vs.* RHE) coupled with an overlapped anodic peak $P_1' \cong P_2'$ ($E' = -0.05$ V *vs.* RHE). The cathodic peaks (P_1 and P_2) are linked to the reduction of dicationic DBV^{2+} to the radical monocationic $DBV^{\bullet+}$ and then to uncharged DBV^0, respectively. The anodic peaks (P_1' and P_2') are attributed to the reversed oxidation of the corresponding ions as depicted in Fig. 1b. Details on the electron transfer of DBV can be found elsewhere.[42,43,45] In addition, a tiny wave at $E = -0.1$ V *vs.* RHE is probably caused by a trace of oxygen in the solution.

Based on the electrochemical behavior of G-SiO_2 in DBV^{2+} solution, it is evident that the on-surface pattern formation by viologen on G-SiO_2 will depend on the potential window. This is confirmed by AFM imaging (Fig. 1c–f). At potentials more positive than $E_1 = -0.3$ V *vs.* RHE, *i.e.* at potentials where dicationic viologen (DBV^{2+}) is the dominant species, rinsing with superpure water leads to pristine graphene (RMS surface roughness = 0.27 nm) which is attributed to the high solubility of DBV^{2+} (Fig. 1d). Between $E_1 = -0.3$ V and $E_2 = -0.5$ V *vs.* RHE, DBV^{2+} is electrochemically reduced to the corresponding radical mono-cationic $DBV^{\bullet+}$ species which assembles into a so-called "dimer phase".[41,46] However, also this species is easily removed from the surface upon rinsing with water (Fig. 1e).[46] The remaining topographic features (Fig. 1d and e) are attributed to water-insoluble byproducts, *i.e.* oligomers or polymers, formed by the radical mono-cations.[46] At potentials more negative than $E_2 = -0.5$ V, water-insoluble DBV^0 is the dominant species and hence the G-SiO_2 surface is fully covered by a DBV^0 layer which is water-insoluble (RMS surface roughness = 0.47 nm (Fig. 1f)). At potentials more negative than $E = -0.85$ V, the surface is not homogeneously covered by DBV^0 as disk-shaped molecule-free islands appear, likely caused by the release of hydrogen nanobubbles (see Fig. S1, ESI†).[47,48]

In addition to AFM, we investigated the organization of DBV^0 on G-SiO_2 by ambient STM (Fig. 2). Although the image resolution is inferior compared to the one obtained on graphite with EC-STM (Fig. S2, ESI†), we can conclude that also DBV^0 self-assembles on G-SiO_2 into the so-called stacking phase as marked by black lines in Fig. 2b, and this phase remains intact even in absence of electrochemical control. This observation demonstrates that the G-SiO_2 surface is permanently functionalized by the self-assembled stacking pattern of DBV^0.

Having established by AFM and STM that tunable patterning of the viologen species on G-SiO_2 is possible we now aim to explore their doping effect with respect to graphene, a zero band gap material. The conduction band edge of graphene is at around 0 V while the reduction potentials of DBV are −0.5 V ($DBV^0/DBV^{\bullet+}$) and −0.28 V ($DBV^{\bullet+}/DBV^{2+}$) *vs.* RHE. Hence graphene may act as the electron-accepting material in presence of DBV^0.[49] In order to determine the degree of doping caused by DBV^0 self-assembled on G-SiO_2 a combination of KPFM and Raman spectroscopy was performed on pristine and DBV^0 functionalized G-SiO_2. Note that we refrained to use

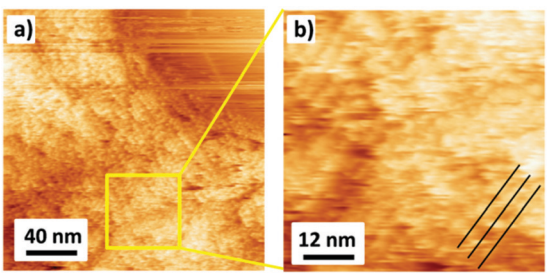

Fig. 2 Ambient STM images show that the stacking phase of the DBV^0 film remains permanently intact after being disconnected from the electrochemical cell; tunneling parameters: $V_b = -0.55$ V, $I_t = 150$ pA.

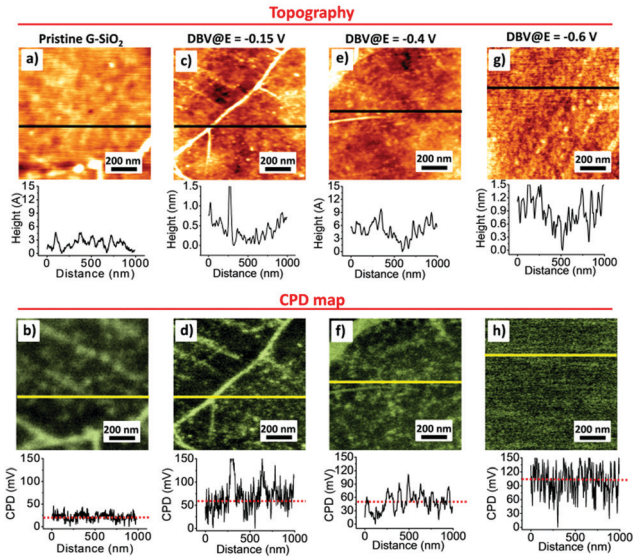

Fig. 3 AFM topographies (a, c, e and g) and corresponding CPD mappings (b, d, f and h) of DBV functionalized G-SiO_2. The electrochemical potential at which G-SiO_2 is functionalized by DBV is indicated on top of the panels.

potentials more negative than $E = -0.85$ V *vs.* RHE to avoid the doping effect caused by hydrogen intercalation.[50–52]

KPFM, an AFM based technique, can be used to characterize the electrostatic properties of (functionalized) graphene at the nanoscale under ambient conditions by measuring the contact potential difference (CPD) between the sample surface and a conducting AFM probe.[53–55] Comparison of the average (over the scanned area) values of CPD obtained for the pristine and functionalized graphene may provide relevant information on the impact of surface functionalization on doping. Mapping of the CPD distribution characterizes the degree of spatial homogeneity of the surface potential within the scanned area.

Fig. 3 shows the surface morphologies and the corresponding CPD maps obtained for pristine G-SiO_2 and G-SiO_2 exposed to DBV at different substrate potentials, *i.e.* $E = -0.15$ V, -0.4 V, and -0.6 V *vs.* RHE. Those DBV-exposed G-SiO_2 samples were rinsed with MQ water and dried with Ar flow before measurement. The presented topographic images show the changes in morphology discussed above associated with electrochemical control. The corresponding KPFM measurements show some differences in the average values of CPD. Whereas the CPD measured on a micrometer scale is in general homogeneous, we see significant local variations attributed to some rare topographic features. For pristine G-SiO_2 (Fig. 3a) as well as for samples prepared at $E = -0.15$ V (Fig. 3c) wrinkles formed during graphene growth and transfer lead to topographically higher features in the AFM image and also a corresponding higher CPD signal in the KPFM map. This contrast difference in the KPFM images is attributed to a reduced interaction with the SiO_2 substrate and multilayer character of the folds (Fig. 3b, d and Fig. S3, ESI†).[56]

The CPD signal depends on the amount and nature of DBV deposited on G-SiO_2. For samples prepared at $E = -0.15$ V (Fig. 3c) and $E = -0.4$ V (Fig. 3e), G-SiO_2 is either not functionalized or covered by oligomers/polymers formed by $DBV^{\bullet+}$. Taking into account the scatter of $\pm$ 30 mV obtained form the CPD histogram (Fig. S4b, ESI†) the CPD values (Fig. 3d and f) are similar to those of pristine G-SiO_2, although local variations of CPD is considerably larger. In contrast, samples prepared at $E = -0.6$ V where DBV^0 is the dominant species (Fig. 3g and h), the surface potential is shifted by $\sim$95 $\pm$ 30 mV to more positive values (Fig. S4b, ESI†) relative to the surface potential value of pristine G-SiO_2. At $E = -0.85$ V, this relative positive shift in surface potential is reduced to $\sim$30 mV (Fig. S5a and b, ESI†). This may be caused by a reduced surface coverage by DBV^0 due hydrogen bubbling (Fig. S1a and b, ESI†). Note that an accurate quantitative estimation of the surface potential values may be affected by contaminants as well as water dipoles formed at the interface.[57] However, our results show that by changing the working electrode's potential the amount of DBV^0 deposited on G-SiO_2 is tunable, as well as the surface potential of graphene. DBV^0 has one of the lowest reduction potentials[58] and hence electron transfer to graphene inducing n-doping is feasible.[3,37,49]

Having established by KPFM how the electrical properties of graphene change upon exposure to DBV^0, the potential controlled electron donating effect was also studied by Raman spectroscopy.

Raman measurements were conducted on G-SiO_2 samples before and after functionalization with DBV at selected potentials, *i.e.*, $E = -0.15$ V, -0.40 V, and -0.6 V *vs.* RHE. Raman maps (10×10 μm^2, 10×10 pixels) were recorded at 3 different locations on each sample. Based on the position shifts of the two characteristic Raman bands of graphene, *i.e.*, the G and 2D bands, the level of doping upon functionalization can be determined. Compared to charge neutral graphene, the G band shifts to higher wave numbers upon p- and n-type doping, while the 2D band shifts to higher wave numbers for p-type doping and lower for high amounts of n-type doping. However, apart from the charge carrier concentration, also strain affects the position of both bands. To separate both effects, analysis is performed on the correlation between their positions.[59] This analysis is based on the approximately linear dependence of the position of both bands on strain and p-type doping, where the 2D band position (Pos(2D)) is more sensitive to strain compared to the position of the G band (Pos(G)), while for doping the sensitivity is opposite. Consequently, in a plot of Pos(2D) *versus* Pos(G), the changes in doping and strain result in linear shifts of the 2D band in relation to the G band position, where the slopes of Pos(2D) *verus* Pos(G) are 0.7 $\pm$ 0.05 and 2.2 $\pm$ 0.2, respectively. Therefore, shifts in the peak positions in a plot of Pos(2D) and Pos(G) along a line with a slope of $\approx$2.2 correspond to a variation in strain, while a slope of $\approx$0.7 indicates doping.

Fig. 4 shows Raman spectra and plots of the 2D peak *versus* the G peak positions for pristine and functionalized G-SiO_2. For pristine graphene, Pos(G) is around 1600 cm^{-1}, which is at significantly higher wave numbers compared to charge neutral graphene (1581.5 cm^{-1}). This upshift indicates that G-SiO_2 is heavily p-type doped due to water and oxygen adsorbed on the surface and/or trapped between graphene and SiO_2.[59] To

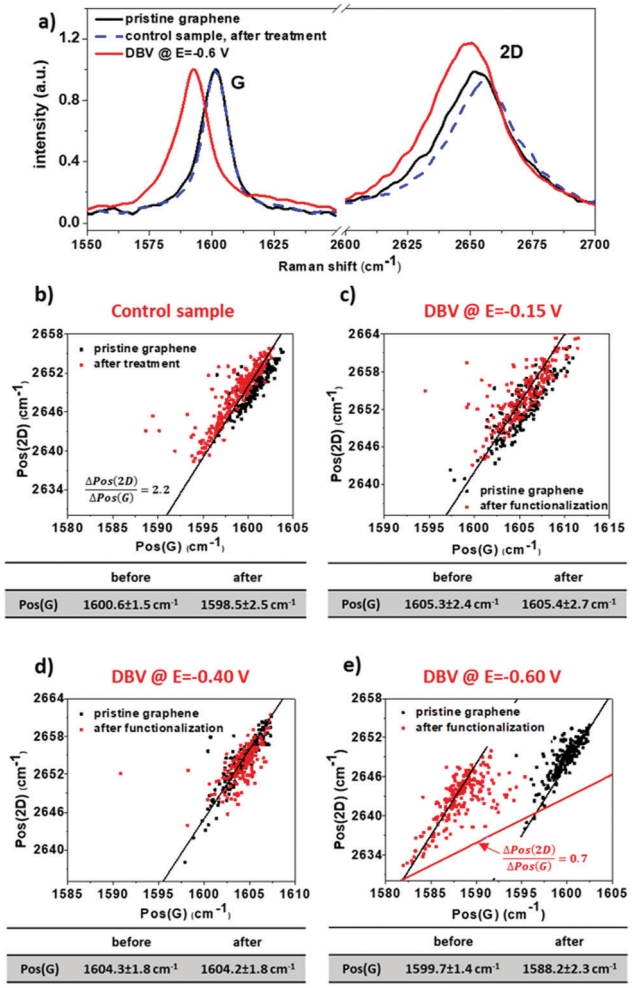

Fig. 4 (a) Raman spectra and (b–e) plots of Pos(2D) *versus* Pos(G) of G-SiO_2 samples before and after electrodeposition of DBV. The electrochemical potential at which G-SiO_2 is functionalized by DBV is indicated on top of the panels. The black lines in (b–e) have a slope of 2.2 and highlight the variation in strain and the red guideline in (e) indicates the direction in shift of the data points upon doping.

establish the impact of exposure to DBV-free electrolyte, Raman mapping was carried out on G-SiO_2 exposed for 180s to the supporting electrolyte (10 mM HCl) at the polarization potential $E = -0.6$ V *vs.* RHE. After this treatment, the Raman data show a negligible difference in both the position of the G-band and 2D-band (Fig. 4a and b). Therefore, any change in the position of these peaks for G-SiO_2 substrates exposed to DBV containing electrolyte can be attributed to the effect of DBV.

Fig. 4c illustrates the plots of Pos(2D) *versus* Pos(G) of G-SiO_2 before and after exposure to DBV containing electrolyte. Note that for all measurements, the spread of the data points follows a line with a slope of approximately 2.2, which is caused by strain variations in graphene.[60] No shift was detected for samples polarized at $E = -0.15$ V and $E = -0.4$ V, respectively (Fig. 4c and d). However, a significant red shift in Pos(G) (11.5 ± 1.5 cm^{-1}), was observed with samples polarized at $E = -0.6$ V (Fig. 4a and e). This shift indicates a reduction in p-type doping and therefore a net n-type doping effect after functionalization. In addition to a shift of Pos(G), the n-type doping is corroborated by an increase of the intensity ratio of the 2D *versus* the G band and an increase of the full width at half maximum of the G band (Table S1, ESI†) after functionalization. Using experimental data in ref. 61, the number of electrons injected into graphene can be estimated to be approximately 8×10^{12} cm^{-2}.[61] The results are attributed to the homogeneous coverage of DBV^0 on G-SiO_2. Furthermore, no significant increase in D band intensity was observed after functionalization with DBV, demonstrating that the electrodeposition process does not induce defects in graphene (Fig. S6 and Table S1, ESI†). A smaller red shift in Pos(G) (7.8 ± 1.2 cm^{-1}) for the sample prepared at $E = -0.85$ V (Fig. S5c, ESI†), is attributed to a reduced DBV^0 coverage due to hydrogen evolution reaction at this potential.

In combination with the positive shift of the surface potential as revealed by KPFM, the red shift of the G peak supports an n-type doping effect caused by adsorbed DBV^0 molecules. It is worth emphasizing that in comparison with other methods employed to dope graphene by viologens[3,37,49] our approach has the advantage of easy control of the doping level due to its one-step protocol and redox state controlled self-assembly process in a compact environment.

Conclusions

We have demonstrated a one-step process to form a self-assembled adlayer of DBV^0 that can be used as n-type dopant for CVD graphene. Upon controlling the electrochemical potential, conditions are generated where exclusively DBV^0 molecules are deposited in a self-assembled manner on G-SiO_2. The film morphology and n-type doping effect of DBV^0 was elucidated using a combination of STM, AFM, KPFM and Raman spectroscopy. This non-destructive bottom-up strategy opens up a new avenue to dope graphene by organic self-assembled adlayers using redox-active molecules under electrochemical control.

Author contributions

H. T. M. T. and T. H. P. prepared the samples. H. T. M. T. conducted and analyzed the CV, STM and EC-STM data. T. H. P. recorded and analyzed the AFM data. R. P. performed and analyzed the Raman data. A. V. performed KPFM measurements. T. M. T. H. and S. D. F. conceived and designed the work. T. H. P., T. M. T. H., and S. D. F. cowrote the paper. All authors contributed to the discussion of the results and commented on the manuscript.

Conflicts of interest

The authors declare no competing financial interest.

Acknowledgements

This research is funded by Vietnam National Foundation for Science and Technology Development (Nafosted) under grant number 104.05-2019.52. S. D. F. gratefully acknowledges financial support from the Fund of Scientific Research Flanders (FWO), KU Leuven – Internal Funds (C14/19/079) and EOS 30489208.

Notes and references

1 A. K. Geim, *Science*, 2009, **324**, 1530.
2 K. S. Novoselov, A. K. Geim, S. V. Morozov, D. Jiang, Y. Zhang, S. V. Dubonos, I. V. Grigorieva and A. A. Firsov, *Science*, 2004, **306**, 666–669.
3 H. K. Jeong, K.-j. Kim, S. M. Kim and Y. H. Lee, *Chem. Phys. Lett.*, 2010, **498**, 168–171.
4 X. Chen, X. Duan, W.-D. Oh, P.-H. Zhang, C.-T. Guan, Y.-A. Zhu and T.-T. Lim, *Appl. Catal., B*, 2019, **253**, 419–432.
5 P. Joshi, H.-H. Huang, R. Yadav, M. Hara and M. Yoshimura, *Catal. Sci. Technol.*, 2020, **10**, 6599–6610.
6 R. Pawlak, X. Liu, S. Ninova, P. D'Astolfo, C. Drechsel, S. Sangtarash, R. Häner, S. Decurtins, H. Sadeghi, C. J. Lambert, U. Aschauer, S.-X. Liu and E. Meyer, *J. Am. Chem. Soc.*, 2020, **142**, 12568–12573.
7 H. Xu, L. Ma and Z. Jin, *J. Energy Chem.*, 2018, **27**, 146–160.
8 M. Z. Hossain, M. A. Walsh and M. C. Hersam, *J. Am. Chem. Soc.*, 2010, **132**, 15399–15403.
9 Z. Qiu, J. Yu, P. Yan, Z. Wang, Q. Wan and N. Yang, *ACS Appl. Mater. Interfaces*, 2016, **8**, 28291–28298.
10 Z. Xia, F. Leonardi, M. Gobbi, Y. Liu, V. Bellani, A. Liscio, A. Kovtun, R. Li, X. Feng, E. Orgiu, P. Samorì, E. Treossi and V. Palermo, *ACS Nano*, 2016, **10**, 7125–7134.
11 J. Greenwood, T. H. Phan, Y. Fujita, Z. Li, O. Ivasenko, W. Vanderlinden, H. Van Gorp, W. Frederickx, G. Lu, K. Tahara, Y. Tobe, H. Uji-i, S. F. L. Mertens and S. De Feyter, *ACS Nano*, 2015, **9**, 5520–5535.
12 T. H. Phan, H. Van Gorp, Z. Li, T. M. Trung Huynh, Y. Fujita, L. Verstraete, S. Eyley, W. Thielemans, H. Uji-i, B. E. Hirsch, S. F. L. Mertens, J. Greenwood, O. Ivasenko and S. De Feyter, *ACS Nano*, 2019, **13**, 5559–5571.
13 K. Fan, X. Liu, Y. Liu, Y. Li, Y. Chen, Y. Meng, X. Liu, W. Feng and L. Luo, *Carbon*, 2020, **167**, 826–834.
14 C. Meng, Q. Chen, X. Li and H. Liu, *J. Membr. Sci.*, 2019, **582**, 83–90.
15 K. R. Nandanapalli, D. Mudusu and S. Lee, *Carbon*, 2019, **152**, 954–985.
16 G. Ambrosio, A. Brown, L. Daukiya, G. Drera, G. Di Santo, L. Petaccia, S. De Feyter, L. Sangaletti and S. Pagliara, *Nanoscale*, 2020, **12**, 9032–9037.
17 H. Wang, T. Maiyalagan and X. Wang, *ACS Catal.*, 2012, **2**, 781–794.
18 B. Cai, S. Zhang, Z. Yan and H. Zeng, *ChemNanoMat*, 2015, **1**, 542–557.
19 T. Torres, *Chem. Soc. Rev.*, 2017, **46**, 4385–4386.
20 A. Lopez and J. Liu, *Adv. Intell. Syst.*, 2020, **2**, 2000123.
21 M. Gobbi, S. Bonacchi, J. X. Lian, Y. Liu, X.-Y. Wang, M.-A. Stoeckel, M. A. Squillaci, G. D'Avino, A. Narita, K. Müllen, X. Feng, Y. Olivier, D. Beljonne, P. Samorì and E. Orgiu, *Nat. Commun.*, 2017, **8**, 14767.
22 A. Ciesielski and P. Samorì, *Adv. Mater.*, 2016, **28**, 6030–6051.
23 K. S. Mali, J. Greenwood, J. Adisoejoso, R. Phillipson and S. De Feyter, *Nanoscale*, 2015, **7**, 1566–1585.
24 K. Madasamy, D. Velayutham, V. Suryanarayanan, M. Kathiresan and K.-C. Ho, *J. Mater. Chem. C*, 2019, **7**, 4622–4637.
25 G. Huseynova, N. K. Shrestha, Y. Xu, E.-Y. Shin, W.-T. Park, D. Ji and Y.-Y. Noh, *Org. Electron.*, 2018, **62**, 572–580.
26 K. W. Shah, S.-X. Wang, D. X. Y. Soo and J. Xu, *Polymers*, 2019, **11**, 1839.
27 Z. Mi, T. Zhou, W. Weng, J. Unruangsri, K. Hu, W. Yang, C. Wang, K. A. I. Zhang and J. Guo, *Angew. Chem., Int. Ed.*, 2021, **60**, 9642–9649.
28 B. A. MacLeod, N. J. Stanton, I. E. Gould, D. Wesenberg, R. Ihly, Z. R. Owczarczyk, K. E. Hurst, C. S. Fewox, C. N. Folmar, K. Holman Hughes, B. L. Zink, J. L. Blackburn and A. J. Ferguson, *Energy Environ. Sci.*, 2017, **10**, 2168–2179.
29 S. Y. Lee, S. W. Lee, S. M. Kim, W. J. Yu, Y. W. Jo and Y. H. Lee, *ACS Nano*, 2011, **5**, 2369–2375.
30 W. J. Yu, L. Liao, S. H. Chae, Y. H. Lee and X. Duan, *Nano Lett.*, 2011, **11**, 4759–4763.
31 V. Rebuttini, E. Fazio, S. Santangelo, F. Neri, G. Caputo, C. Martin, T. Brousse, F. Favier and N. Pinna, *Chem. – Eur. J.*, 2015, **21**, 12465–12474.
32 H. Ren, Y. Zhou, Y. Wang, X. Zhu, C. Gao and Y. Guo, *Sens. Actuators, B*, 2020, **321**, 128520.
33 K. Matsuyama, A. Fukui, K. Miura, H. Ichimiya, Y. Aoki, Y. Yamada, A. Ashida, T. Yoshimura, N. Fujimura and D. Kiriya, *ChemistryOpen*, 2019, **8**, 908–914.
34 K. Jo, J. Choi and H. Kim, *J. Mater. Chem. C*, 2017, **5**, 5395–5401.
35 B. Chamlagain, S. S. Withanage, A. C. Johnston and S. I. Khondaker, *Sci. Rep.*, 2020, **10**, 12970.
36 S. Kim, C. Kim, Y. H. Hwang, S. Lee, M. Choi and B.-K. Ju, *Chem. Phys. Lett.*, 2021, **770**, 138453.
37 S. Y. Lee, D. L. Duong, Q. A. Vu, Y. Jin, P. Kim and Y. H. Lee, *ACS Nano*, 2015, **9**, 9034–9042.
38 M. Wilms, M. Kruft, G. Bermes and K. Wandelt, *Rev. Sci. Instrum.*, 1999, **70**, 3641–3650.
39 I. Horcas, R. Fernández, J. M. Gómez-Rodríguez, J. Colchero, J. Gómez-Herrero and A. M. Baro, *Rev. Sci. Instrum.*, 2007, **78**, 013705.
40 R. Phillipson, C. J. Lockhart de la Rosa, J. Teyssandier, P. Walke, D. Waghray, Y. Fujita, J. Adisoejoso, K. S. Mali, I. Asselberghs, C. Huyghebaert, H. Uji-i, S. De Gendt and S. De Feyter, *Nanoscale*, 2016, **8**, 20017–20026.
41 T. M. T. Huynh, T. H. Phan, O. Ivasenko, S. F. L. Mertens and S. De Feyter, *Nanoscale*, 2017, **9**, 362–368.
42 T. H. Phan and K. Wandelt, *Beilstein J. Org. Chem.*, 2014, **10**, 2243–2254.

43 D.-T. Pham, K. Gentz, C. Zörlein, N. T. M. Hai, S.-L. Tsay, B. Kirchner, S. Kossmann, K. Wandelt and P. Broekmann, *New J. Chem.*, 2006, **30**, 1439–1451.
44 C. L. Bird and A. T. Kuhn, *Chem. Soc. Rev.*, 1981, **10**, 49–82.
45 D.-T. Pham, S.-L. Tsay, K. Gentz, C. Zoerlein, S. Kossmann, J.-S. Tsay, B. Kirchner, K. Wandelt and P. Broekmann, *J. Phys. Chem. C*, 2007, **111**, 16428–16436.
46 S. Breuer, D. T. Pham, S. Huemann, K. Gentz, C. Zoerlein, R. Hunger, K. Wandelt and P. Broekmann, *New J. Phys.*, 2008, **10**, 125033.
47 L. Zhang, Y. Zhang, X. Zhang, Z. Li, G. Shen, M. Ye, C. Fan, H. Fang and J. Hu, *Langmuir*, 2006, **22**, 8109–8113.
48 F. Hui, B. Li, P. He, J. Hu and Y. Fang, *Electrochem. Commun.*, 2009, **11**, 639–642.
49 D. Kiriya, M. Tosun, P. Zhao, J. S. Kang and A. Javey, *J. Am. Chem. Soc.*, 2014, **136**, 7853–7856.
50 I. Takuya, S. Jian, K. Nozomu, C. Takuo, A. Masashi, M. Manoharan and M. Hiroshi, *Appl. Phys. Express*, 2015, **8**, 015101.
51 S. Y. Davydov, *Semiconductors*, 2017, **51**, 640–644.
52 J. Grzonka, I. Pasternak, P. P. Michałowski, V. Kolkovsky and W. Strupinski, *Appl. Surf. Sci.*, 2018, **447**, 582–586.
53 X. Zhou, S. He, K. A. Brown, J. Mendez-Arroyo, F. Boey and C. A. Mirkin, *Nano Lett.*, 2013, **13**, 1616–1621.
54 C. Barth, A. S. Foster, C. R. Henry and A. L. Shluger, *Adv. Mater.*, 2011, **23**, 477–501.
55 Y. Shi, K. K. Kim, A. Reina, M. Hofmann, L.-J. Li and J. Kong, *ACS Nano*, 2010, **4**, 2689–2694.
56 F. Long, P. Yasaei, R. Sanoj, W. Yao, P. Král, A. Salehi-Khojin and R. Shahbazian-Yassar, *ACS Appl. Mater. Interfaces*, 2016, **8**, 18360–18366.
57 M. C. R. González, P. Carro, L. Vázquez and A. H. Creus, *Phys. Chem. Chem. Phys.*, 2016, **18**, 29218–29225.
58 S. M. Kim, J. H. Jang, K. K. Kim, H. K. Park, J. J. Bae, W. J. Yu, I. H. Lee, G. Kim, D. D. Loc, U. J. Kim, E.-H. Lee, H.-J. Shin, J.-Y. Choi and Y. H. Lee, *J. Am. Chem. Soc.*, 2009, **131**, 327–331.
59 S. Ryu, L. Liu, S. Berciaud, Y.-J. Yu, H. Liu, P. Kim, G. W. Flynn and L. E. Brus, *Nano Lett.*, 2010, **10**, 4944–4951.
60 C. Neumann, S. Reichardt, P. Venezuela, M. Drögeler, L. Banszerus, M. Schmitz, K. Watanabe, T. Taniguchi, F. Mauri, B. Beschoten, S. V. Rotkin and C. Stampfer, *Nat. Commun.*, 2015, **6**, 8429.
61 M. Bruna, A. K. Ott, M. Ijäs, D. Yoon, U. Sassi and A. C. Ferrari, *ACS Nano*, 2014, **8**, 7432–7441.

